Rapid Communications

Electrical switching of perpendicular magnetization in a single ferromagnetic layer

Liang Liu,[1,*] Jihang Yu,[1,*] Rafael González-Hernández,[2,3] Changjian Li,[1] Jinyu Deng,[1] Weinan Lin,[1] Chenghang Zhou,[1] Tiejun Zhou,[1] Jing Zhou,[1] Han Wang,[1] Rui Guo,[1] Herng Yau Yoong,[1] Gan Moog Chow,[1] Xiufeng Han,[4] Bertrand Dupé,[2,†] Jakub Železný,[5] Jairo Sinova,[2] and Jingsheng Chen[1,6,‡]

[1]*Department of Materials Science and Engineering, National University of Singapore, Singapore 117575*
[2]*Institut für Physik, Johannes Gutenberg Universität Mainz, D-55099 Mainz, Germany*
[3]*Department of Physics, Universidad del Norte, Barranquilla, Colombia*
[4]*Beijing National Laboratory for Condensed Matter Physics, Institute of Physics, Chinese Academy of Sciences, Beijing 100190, China*
[5]*Institute of Physics of the Czech Academy of Sciences, Cukrovarnická 10/112, Prague 16200, Czech Republic*
[6]*Suzhou Research Institute, National University of Singapore, Suzhou 215123, China*

(Received 27 November 2019; revised manuscript received 21 April 2020; accepted 14 May 2020; published 2 June 2020)

We report on the efficient spin-orbit torque (SOT) switching in a single ferromagnetic layer induced by a new type of inversion asymmetry, the composition gradient. The SOT of 6- to 60-nm epitaxial FePt thin films with a $L1_0$ phase is investigated. The magnetization of the FePt single layer can be reversibly switched by applying electrical current with a moderate current density. Different from previously reported SOTs which either decreases with or does not change with the film thickness, the SOT in FePt increases with the film thickness. We found the SOT in FePt can be attributed to the composition gradient along the film normal direction. A linear correlation between the SOT and the composition gradient is observed. This Rapid Communication introduces a platform to engineer large SOTs for lower-power spintronics.

DOI: 10.1103/PhysRevB.101.220402

Electrical manipulation of magnetization through spin-orbit torque (SOT) has been widely investigated in multilayer heterostructures and bulk noncentrosymmetric conductors/semiconductors [1]. For multilayer heterostructures, such as heavy metal/ferromagnet (HM/FM) bilayers, the SOT is considered to arise from the spin Hall effect (SHE) in the HM [2–4] and/or the Rashba effect at the interfaces [5–7]. According to the scenario of the SHE, a spin current generated from the HM is transferred to the FM, exerting a spin-transfer torque on the FM. The torque efficiency is, therefore, significantly dependent on the spin current transmission transparency [8] and the spin relaxation [9] at the HM/FM interface. The Rashba effect in HM/FM bilayers arises from the structural inversion asymmetry. With the Rashba spin-orbit interaction, nonequilibrium spin density of conduction electrons is generated in the FM near the interface, which couples with the magnetic moments. For both effects in HM/FM bilayers, the induced SOT has an *interface* nature, which usually requires a thin FM layer, and makes it challenging to achieve high thermal stability at a small size. On the other side, for bulk noncentrosymmetric conductors/semiconductors which are usually a single-layer crystal, SOT has also been reported. Researchers observed current-induced magnetization switching in thick ferromagnetic semiconductors, such as (Ga,Mn)As (10–15 nm) [10] and (Ge,Mn)Te (22–144 nm) [11] with bulk inversion asymmetry and in thick antiferromagnetic metals CuMnAs (40–80 nm) [12] and Mn_2Au (75 nm) [13] with locally broken inversion symmetry. In these single-layer magnetic crystals, the current-induced spin polarization is uniformly generated in the bulk so that a spin torque is directly exerted on the magnetic moments. Therefore, single-layer SOT has no thickness limitation due to its *bulk* nature. However, for single-layer antiferromagnetic CuMnAs [12] and Mn_2Au [13], the switching is on the film plane, which is not conducive for ultra-high-density magnetic memories. For ferromagnetic semiconductors, the reported SOT switching cannot be achieved at room temperature due to the low transition temperature [10,11,14]. In this Rapid Communication, we demonstrate the observation of the room-temperature SOT switching in a single-layer ferromagnet ($L1_0$ FePt). The efficient electrical switching in $L1_0$ FePt will be of high interest for the practical application because it enables memory cells with sufficient thermal stability to scale down to 3 nm due to its ultrahigh perpendicular magnetic anisotropy (PMA) [15].

$L1_0$ FePt is a face-centered tetragonal structure [Fig. 1(a)] with lattice constant c slightly smaller than lattice constant a ($c/a = 0.968$). Fe and Pt atoms are alternately stacked along the c axis ([001] direction). In our experiment, $L1_0$-ordered FePt films with high PMA were epitaxially grown on different substrates (or buffer layer): $SrTiO_3$ (STO), MgO, and MgO with a 5-nm TiN seed layer (see the Supplemental Material [16]). The $L1_0$ phase and PMA are confirmed by x-ray-diffraction patterns and magnetic hysteresis loops, respectively (see the Supplemental Material [16]). Figure 1(b)

[*]These authors contributed equally to this work.
[†]Fonds de la Recherche Scientifique (FNRS), Bruxelles, Belgium; Nanomat/Q-mat/CESAM, Universite de Liege, B-4000 Sart Tilman, Belgium.
[‡]msecj@nus.edu.sg

 ©2020 American Physical Society

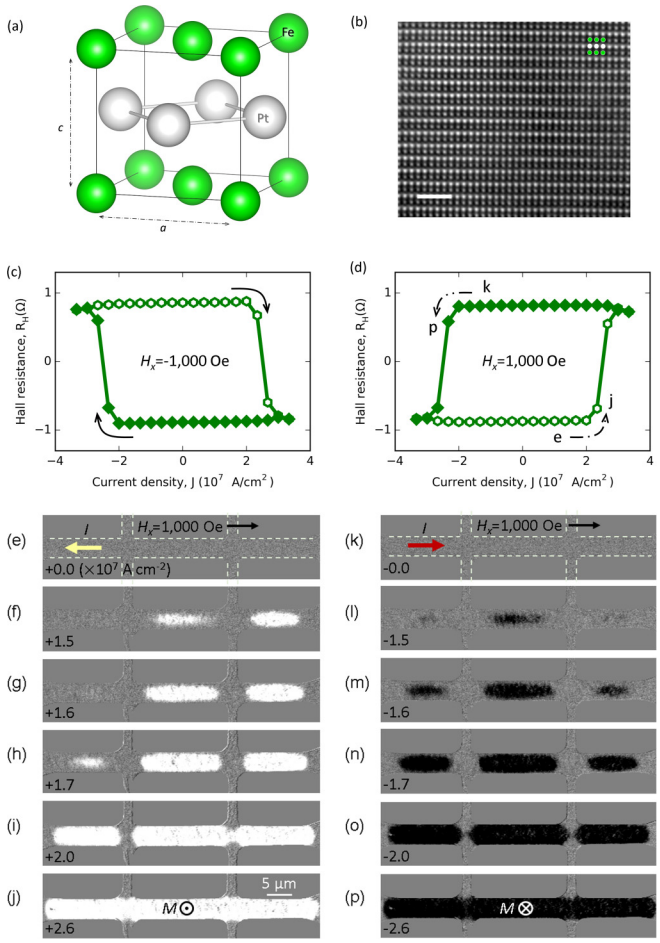

FIG. 1. Current-induced magnetization switching in the $L1_0$ FePt single layer. (a) Crystal structure of $L1_0$ FePt. (b) Scanning transmission electron microscopy (STEM) image of the FePt film in the [100]-[001] plane. The brighter atoms are Pt whereas the darker atoms are Fe. The scale bar is 2 nm. (c) and (d) Current-induced magnetization switching in the 6-nm FePt film on $SrTiO_3$ under in-plane magnetic fields of (c) −1000 Oe and (d) 1000 Oe. (e)–(j) Polar MOKE images showing the magnetization switching process by increasing I_{pulse} from 0 to 2.6×10^7 A/cm^2. The light dashed lines in (e) indicate the Hall bar edges. (k)–(p) Polar MOKE images showing the magnetization switching process by changing I_{pulse} from 0 to -2.6×10^7 A/cm^2. The corresponding processes of (e)–(j) and (k)–(p) are indicated by the arrows in (d).

shows a typical cross-sectional STEM image of our deposited FePt films on TiN/MgO, and a well-defined atomically layered structure is observed. The films on different substrates was patterned into 5-μm Hall bars for transport and optical measurements. A dc pulsed current I_{pulse} with a duration of 30 μs was applied to drive the magnetization switching. Each value of Hall resistance ($R_H = V_{ac}/I_{ac}$) was measured by a small ac current ($I_{ac} < 50\,\mu$A) with 8 s after each pulse. As shown in Fig. 1(c) with an in-plane magnetic field ($H_x = -1000$ Oe) opposite to the current direction, we observe a clockwise switching loop by sweeping I_{pulse}. The polarity of the switching loop reverses after the magnetic field is reversed ($H_x = +1000$ Oe) as shown in Fig. 1(d), indicating a typical current-induced switching behavior similar to that obtained in other SOT bilayers [4,17–20]. By comparing the switching loop in Fig. 1(d) with the anomalous Hall loop in Fig. S2(b) of the Supplemental Material [16], we found a partial switching behavior. This is quite similar to the partial switching observed in single-layer SOT switching of (Ge,Mn)Te [11]. The possible reason for that is the current-induced temperature rise during SOT switching, which reduces the magnetization according to the *M-T* characteristics. In order to directly "see" the magnetization switching process, we use a polar magneto-optic Kerr effect (MOKE) microscopy to capture the magnetization evolution of FePt. The same as in Fig. 1(d), we apply a positive in-plane field ($H_x = +1000$ Oe). Figures 1(e)–1(j) and 1(k)–1(p) show the magnetization evolutions after applying positive and negative I_{pulse}'s, respectively. The switching first happens at the center of the current path [Figs. 1(f) and 1(l)] where the current density is higher than that of the Hall crossing area because of less current shunting effect. The switched area gradually expands with increasing current density and finally fills the whole current path [Figs. 1(g)–1(j) and 1(m)–1(p)].

To systematically study the current-induced magnetization switching, we measure the field dependence in 6- and 20-nm FePt single layers. Figures 2(a) and 2(b) present the current-induced switching loops under varying H_x. We observe that the switching current density (J_c) decreases with increasing amplitude of H_x as summarized in Fig. 2(c), and there is no switching loop under zero magnetic field. Therefore, H_x not only breaks the rotational symmetry of the spin torque, but also reduces the switching energy barrier [21]. The switching behavior exists even when H_x reaches as large as 20 kOe, which is consistent with the ultrahigh magnetic anisotropy of $L1_0$ FePt. We also find that J_c for the 20-nm FePt film ($\sim 7.0 \times 10^6$ A/cm^2) is much lower than that for the 6-nm FePt film ($\sim 2.6 \times 10^7$ A/cm^2), which indicates a bulk SOT behavior. More interestingly, because of the multidomain property in FePt Hall bars, intermediate magnetic states are observed. The stable multiple-level switching behavior by electrical current in the 6-nm FePt film is shown in Fig. 2(d), which is consistent with the domain expanding process in the Hall crossing area, as shown in the Supplemental Material [16]. It is worth noting that we also obtained the SOT switching in a $L1_0$ CoPt single layer (see the Supplemental Material [16]). In order to get more understanding, we measured the spin-orbit effective fields.

Harmonic Hall voltage analysis was conducted to estimate the spin-torque efficiency in $L1_0$ FePt [22–25]. We apply a small ac excitation current and measure the first- (V_ω) and second- ($V_{2\omega}$) harmonic signals. The temperature rise due to the current-induced Joule heating is negligible (see the Supplemental Material [16]). Figure 3(a) shows the schematic of the SOT effective fields (ΔH_L and ΔH_T) in FePt. The field dependences of V_ω and $V_{2\omega}$ are shown in Figs. 3(b)–3(d), $V_{2\omega}$ contains thermoelectrical signals due to the temperature gradient in the device [22,25,26] (see the Supplemental Material [16]). After excluding the thermoelectric effects, the effective fields can be determined by the formula [22,24] $\Delta H_{L(T)} = -2\frac{B_{L(T)} \pm 2\xi B_{T(L)}}{1-4\xi^2}$, where $B_{L(T)}$ is defined as $\{\frac{\partial V_{2\omega}}{\partial H} / \frac{\partial^2 V_\omega}{\partial H^2}\}_{H \| L(T)}$. ξ is the ratio of the planar Hall resistance ΔR_{PHE} to the anomalous Hall resistance ΔR_{AHE} (see the Supplemental Material [16]). The ± sign corresponds to magnetization pointing

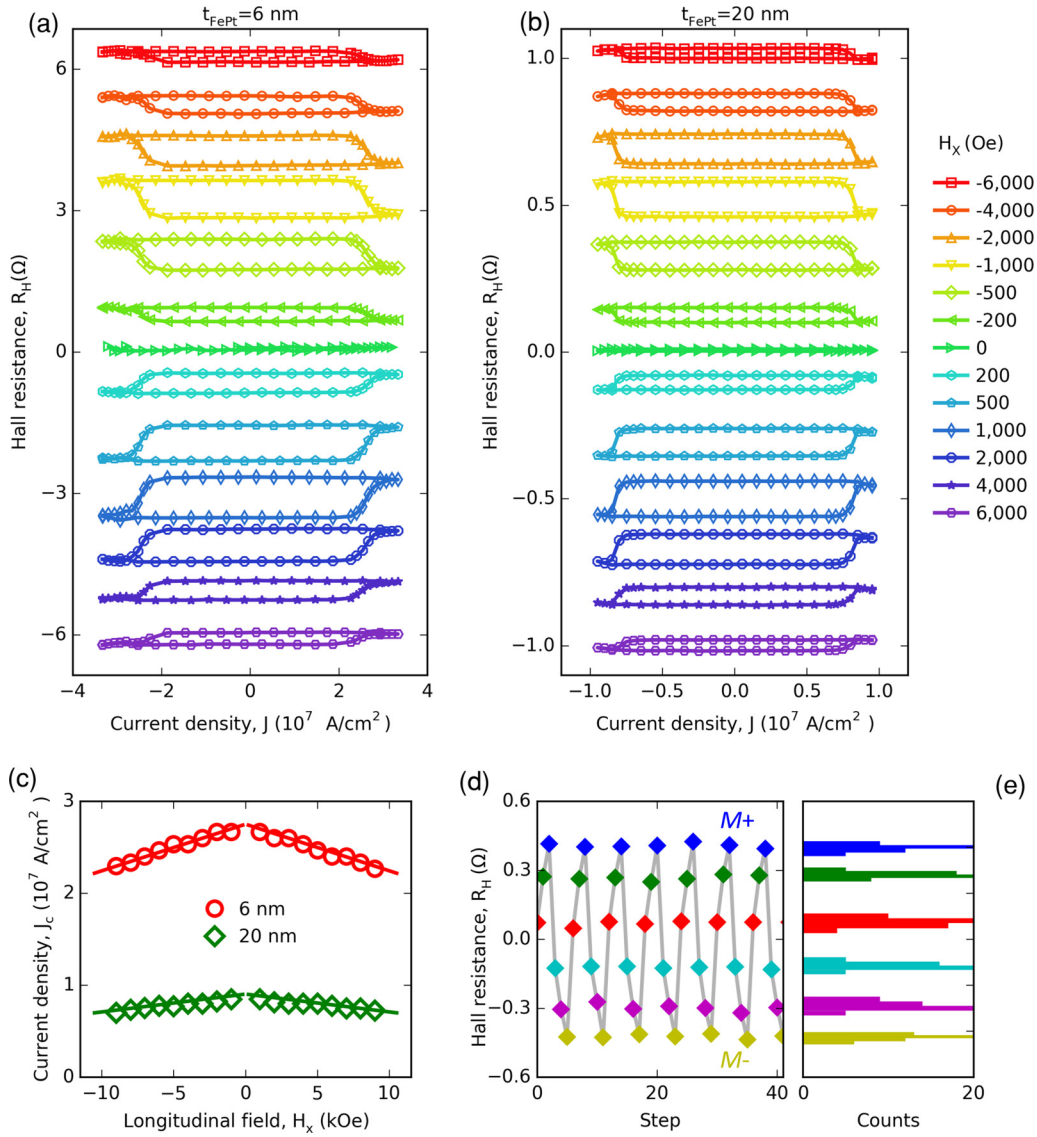

FIG. 2. Field dependence of the SOT switching in FePt on $SrTiO_3$ substrates. (a) and (b) SOT switching loops obtained under varying H_x for (a) 6-nm and (b) 20-nm FePt films. (c) Critical switching current density (J_c) as a function of H_x. (d) Current-induced multilevel switching in 6-nm FePt film with controlled series of current pulses (see the Supplemental Material [16]). Six intermediate states ($-0.45\,\Omega$, $-0.3\,\Omega$, $-0.15\,\Omega$, $0.1\,\Omega$, $0.3\,\Omega$, and $0.4\,\Omega$) are observed. (e) Histogram of the six resistance states in (d), obtained from 50 repetitions of 3 positive + 3 negative pulse current sequence.

along the $\pm z$ axis (i.e., $\pm M$). The symmetries of ΔH_L (odd) and ΔH_T (even) indicate a typical SOT property that is the same as that studied in HM/FM bilayers (see the Supplemental Material [16]). To compare the SOT with that in previous HM/FM bilayers, we calculate the spin-torque efficiencies ($\beta_{L(T)}$), which is defined as $\Delta H_{L(T)}/J_e$. For the 20-nm FePt film, β_L and β_T are 65 and 30 Oe/ (10^7 A/cm^2), respectively. Whereas for the 6-nm FePt film, β_L and β_T are 12 and 5 Oe/ (10^7 A/cm^2), respectively. The SOT in 20-nm FePt is larger than that in 6-nm FePt, which is consistent with the smaller switching current density in 20-nm FePt than that in 6-nm FePt. Next, we study the physics origin of the SOT in FePt.

In general, SOT exists in systems with broken inversion symmetry. $L1_0$ FePt and CoPt have a centrosymmetric bulk space-group *P4/mmm* and a centrosymmetric polar site point-group D_{4h} for Fe (Co) and Pt atoms, which does not allow for the generation of SOT in an ideal $L1_0$-ordered crystal [27]. Therefore, the SOT can only originate from either the interface or the deviation from a perfect $L1_0$ phase in the bulk.

To examine the interface effect, we compare the $\beta_{L(T)}$ values of the 20-nm FePt films on three types of substrates: STO, MgO, and TiN(5 nm)/MgO. Among them, STO and MgO are nonconductive oxides with different lattice mismatches (1.4% and 8.6%) to FePt [28], whereas TiN is a conductive seed layer with a lattice mismatch of 9.2% to FePt. We found the three types of FePt samples have similar β_L's [Fig. 3(e)], whereas their β_T's are different from each other. This result indicates that the interface can affect the SOT (β_T) in FePt but does not play a central role in the current-induced switching behavior which was supposed to be driven by the dampinglike field (β_L). Besides, we found the SOT can be significantly

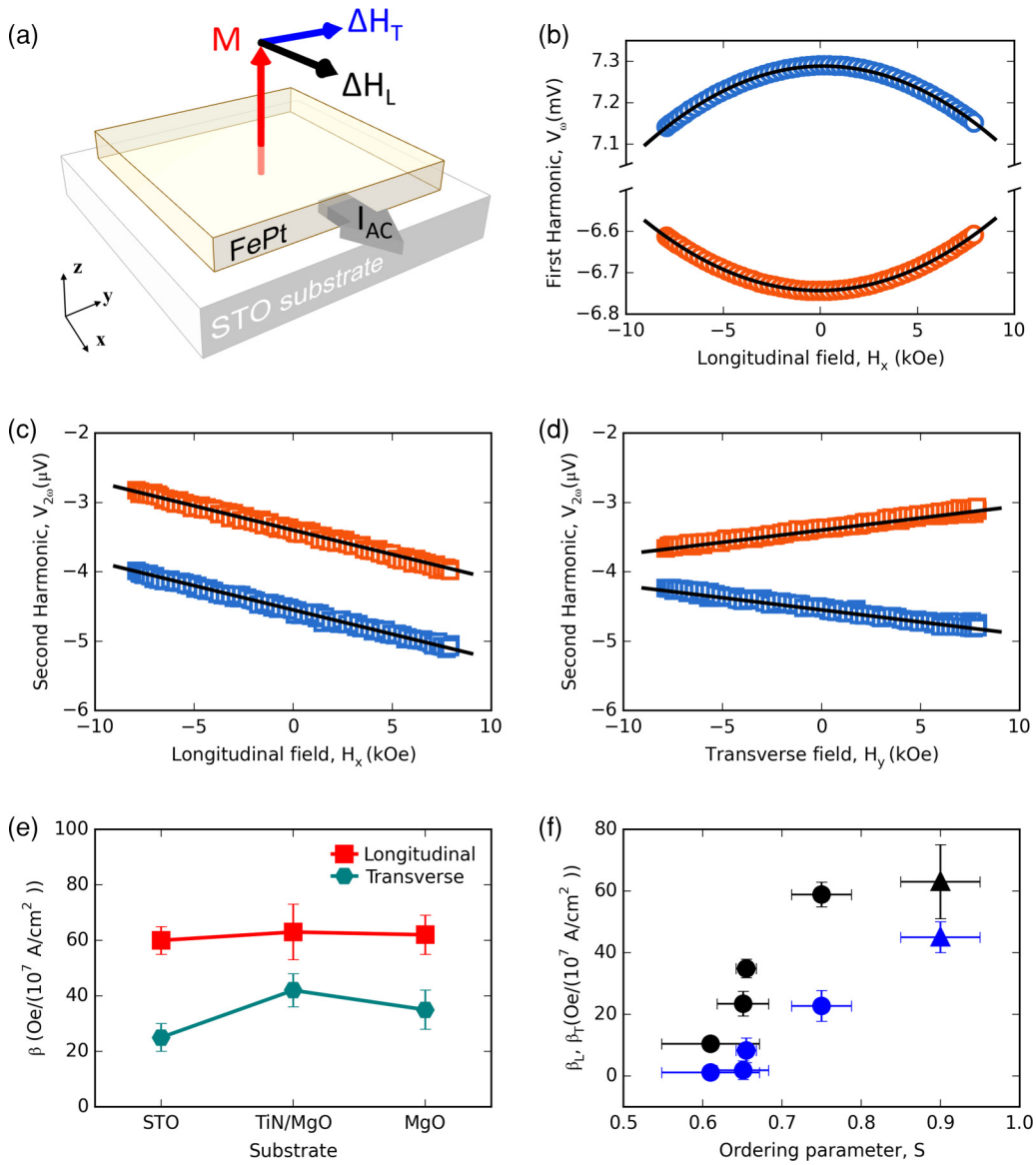

FIG. 3. Estimation of spin-orbit effective fields in 20-nm FePt films by harmonic Hall measurements**.** (a) Schematic of the spin-orbit effective fields in FePt. (b)–(d) Field dependence of (b) first- and (c) and (d) second-harmonic signals for 20-nm FePt film ($I_{ac} = 10$ mA). The blue and orange colors in (b)–(d) correspond to $+M$ and $-M$, respectively. (e) Longitudinal and transverse spin-torque efficiencies for the 20-nm FePt films grown on $SrTiO_3$, MgO, and TiN (5 nm)/MgO substrates. (f) Ordering parameter dependence of longitudinal (dark symbols) and transverse (blue symbols) spin-torque efficiencies in 20-nm FePt films. The round symbols represent FePt films grown on $SrTiO_3$ substrates with different deposition temperatures. The triangular symbols are for the FePt films grown on TiN (5 nm)/MgO substrates.

affected by the chemical ordering parameter (S), which is used to characterize the degree of how many atoms (Fe or Pt) are in the right sites of a $L1_0$ structure. The value of S can be tuned by the deposition temperature of the FePt films. We deposited four 20-nm FePt films on STO substrates at 500 °C, 465 °C, 430 °C, and 400 °C to obtain different values of S (0.75, 0.67, 0.65, and 0.60). We found both β_L and β_T increase with S as shown in Fig. 3(f). We note that the SOT results for the 20-nm FePt film on TiN/MgO were also included in this figure, which has a larger S value (∼0.90). Therefore, the SOT in FePt is closely related to the $L1_0$-ordered structure, which again indicates a *bulk* nature.

After excluding the interface effect, we carefully checked the bulk of the FePt film. To further minimize the interface effect, we focused on thicker (20-, 30-, 40-, 50-, and 60-nm) FePt films on TiN (5 nm)/MgO, which have better epitaxial structures with S larger than 0.9. Figure 4(a) shows a cross-sectional STEM image of the thickest FePt film (60 nm), which gives an overview of the film quality. Figures 4(b) and 4(c) are typical zoom-in images on the top and the bottom, respectively. Both indicate well-arranged atomically layered structures. The film is uniform in these two regions, and it is difficult to identify any inversion asymmetry. However, when we performed the elemental analysis of the two regions, we found that their elemental compositions are quite different: $Fe_{48}Pt_{52}$ and $Fe_{41}Pt_{59}$ for the bottom and top, respectively. We also checked two central regions (2 and 3) as indicated in Fig. S11(a) of the

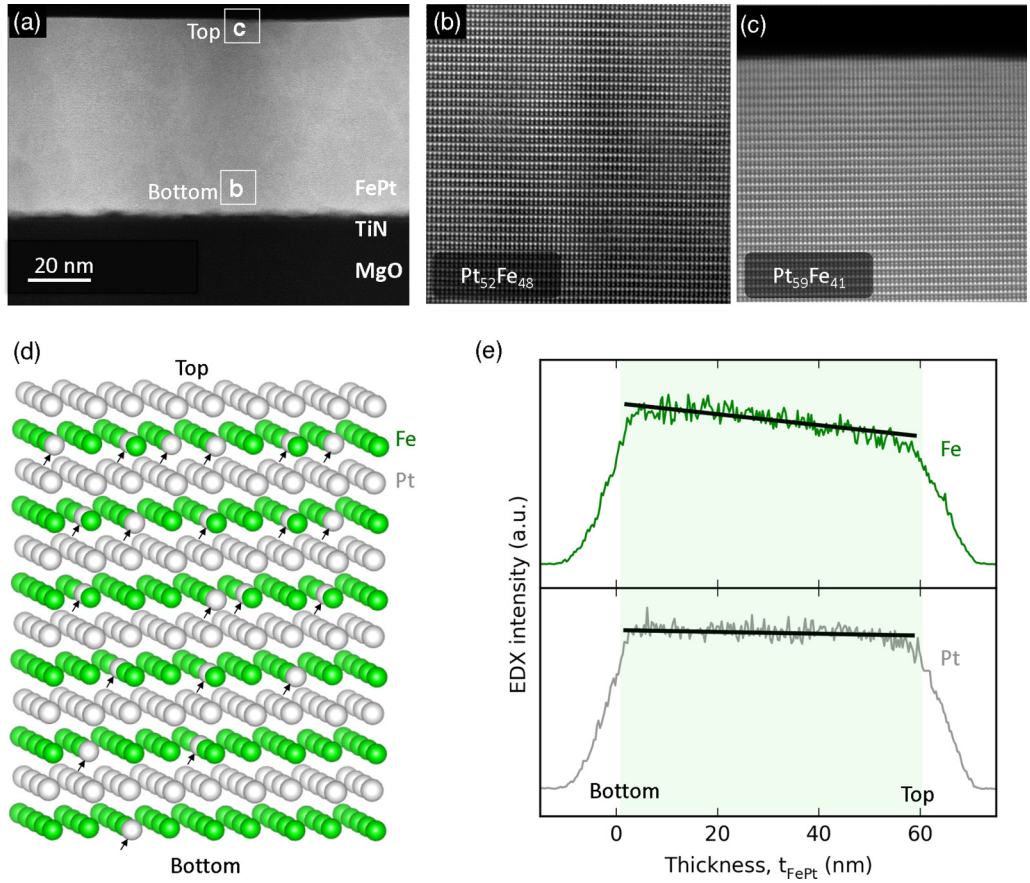

FIG. 4. Composition gradient in the 60-nm FePt film. (a) Cross-sectional high-angle annular dark-field-STEM image of a 60-nm FePt film on TiN (5 nm)/MgO. (b) and (c) Zone-in STEM images at the (b) bottom and the (c) top of the 60-nm FePt film as indicated in (a). The brighter atoms are Pt whereas the darker atoms are Fe. (d) Schematic of a stoichiometry gradient in the FePt structure where certain Fe atoms are replaced by Pt in the Fe atomic layers. (e) Overall energy dispersive x-ray (EDX) intensity along the vertical direction for Fe (upper panel) and Pt (lower panel).

Supplemental Material [16] and found their compositions are $Fe_{45}Pt_{55}$ and $Fe_{43}Pt_{57}$, respectively. The gradual change in the composition (Fig. S11(d) of the Supplemental Material [16]) implies that there is a composition gradient in FePt films. The EDX elemental mappings for Fe (K line) and Pt (L line) across the whole thickness are shown in the Supplemental Material [16] from which we obtained the line profiles of integrated intensities for Fe and Pt [Fig. 4(e)]. Due to the slight wedge shape of the TEM lamella, we found that both the Fe and the Pt signals show decreasing trends with the thickness of FePt. However, the Fe signal decreases with a larger negative slope compared with that of Pt, according to their corresponding linear fits in Fig. 4(e). That means the Pt/Fe ratio increases with the thickness of FePt, and the composition gradient was estimated to be 0.71%/nm (Pt/Fe composition ratio changes about 0.71% per nanometer). As a result, the top surface has less Fe than the bottom regions as illustrated in Fig. 4(d). This composition gradient breaks the inversion symmetry of the structure.

In order to investigate the correlation between the SOT and the composition gradient, we first measured the spin-torque efficiencies as a function of the FePt thickness as shown in Fig. 5(a) We observed that the dampinglike term β_L (the fieldlike term β_T) increases with FePt thickness from 6 to 40 nm (50 nm) and then saturates. The increasing SOT with thickness was not reported before in magnetic bilayers or single layers. According to Fig. 5(a), we chose three FePt films (20, 30, and 60 nm) with different SOTs and obtained their Pt/Fe composition gradients, which are 0.31, 0.53, and 0.71%/nm, respectively (the detailed results are shown in the Supplemental Material [16]). In Fig. 5(b), we plot the spin-torque efficiencies (β_L and β_T) as a function of composition gradient (G) for these three samples where two linear correlations are observed. This finding indicates that the SOT in FePt single layer originates from the composition gradient. Since there is no adjacent HM layer to supply as a spin Hall source, we suggest that the SOT in $L1_0$ FePt should be explained by the inverse spin galvanic effect, which exists in any magnetic system with broken inversion symmetry. However, a detailed description of the microscopic mechanism requires further study. We also note that the $L1_0$ crystal structure plays an important role for the SOT in FePt since the SOT is strongly dependent on the chemical ordering parameter (S). Considered the extreme cases, the A1 fcc FePt is fully disordered with $S = 0$, whereas the ideal $L1_0$ FePt is fully ordered with $S = 1$. In principle, the face-centered-tetragonal structure is lower in symmetry than the face-centered-cubic structure, which might provide a basis for tun-

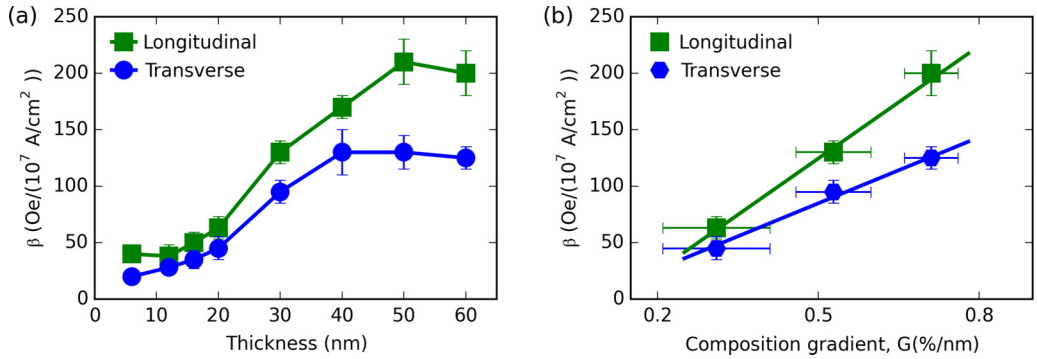

FIG. 5. The dependence of SOT effective fields on composition gradient. (a) Thickness dependence of longitudinal and transverse spin-torque efficiencies for FePt films on TiN (5 nm)/MgO. (b) Longitudinal and transverse spin-torque efficiencies as a function of the composition gradient. The data points are for the 20-, 30-, and 60-nm FePt samples with Pt/Fe composition gradients of 0.31, 0.53, and 0.71%/nm, respectively.

ing the SOT in FePt through the chemical ordering parameter [Fig. 3(f)].

The combination of spin-orbit coupling and inversion symmetry breaking gives rise to emergent phenomena, such as SOT and Dzyaloshinskii-Moriya interaction (DMI). Recently, Kim *et al.* [29] reported that the composition gradient in an amorphous ferrimagnetic alloy (GdFeCo) could break the inversion symmetry and give rise to a bulk DMI. They found that both the DMI and the Gd/Fe composition gradient increase with the film thickness, which is very similar to our experimental results shown here but with the DMI taking the role of the SOT. In their report, the Gd/Fe composition gradient changes from 1 to 3%/nm with the thickness increased from 10 to 50 nm. Whereas in our Rapid Communication, the Pt/Fe composition gradient is several times smaller, which changes from 0.31 to 0.71%/nm with the thickness increased from 20 to 60 nm. The observation of the composition gradient in these two different (crystalline and amorphous) systems indicates a new type of inversion asymmetry which could be largely neglected in previous studies. With this compositional inversion asymmetry, the SOT in FePt behaves very differently compared with that in previous studies considering the thickness dependence. For the inversion asymmetry at the HM/FM interface, the SOT effect should decrease with the FM thickness. For the bulk inversion asymmetry in noncentrosymmetric semiconductors, the SOT is independent of the FM thickness. However, due to the increasing composition gradient with thickness in FePt thin films, the SOT increases with the thickness.

To summarize, we have realized the room-temperature SOT switching in a single ferromagnetic layer (FePt), which makes it a good candidate for ultra-high-density magnetic random access memory due to its much better thermal stability than those previously reported HM/FM bilayers. In previous SOT systems, the inversion symmetry breakings are either structural or geometrical. We show here that the inversion symmetry breaking can also be compositional, which may offer the opportunity to engineer large SOT in a wide range of materials.

The research was supported by the Singapore National Research Foundation under CRP Award No. NRF-CRP10-2012-02 and the Ministry of Education under Awards No. MOE2018-T2-2-043, No. MOE2018-T2-1-019, No. R-284-000-196-114, No. MOE2019-T2-1-150, No. AMEIRG18-0022, and No. A*STAR IAF-ICP 11801E0036. J.C. is the member of the Singapore Spintronics Consortium (SG-SPIN). R.G.-H. and B.D. are grateful for the computing time granted on the supercomputers on Mogon at Johannes Gutenberg Universität of Mainz. J.S., R.G.-H., and B.D. acknowledge financial support from the Alexander von Humboldt Foundation and the Deutsche Forschungsgemeinschaft (DFG, German Research Foundation) - TRR 173 268565370 (project A03). J.S. also acknowledges the Grant Agency of the Czech Republic Grant No. 19-28375X. J.Ž. acknowledges the Grant Agency of the Czech Republic Grant No. 19-18623Y and support from the Institute of Physics of the Czech Academy of Sciences and the Max Planck Society through the Max Planck Partner Group Programme. This work was supported by The Ministry of Education, Youth and Sports from the Large Infrastructures for Research, Experimental Development and Innovations Project, IT4 Innovations National Supercomputing Center, Grant No. LM2015070.

[1] A. Manchon, J. Železný, I. M. Miron, T. Jungwirth, J. Sinova, A. Thiaville, K. Garello, and P. Gambardella, Rev. Mod. Phys. **91**, 035004 (2019).

[2] M. I. Dyakonov and V. I. Perel, Phys. Lett. A **35**, 459 (1971).

[3] J. Sinova, S. O. Valenzuela, J. Wunderlich, C. H. Back, and T. Jungwirth, Rev. Mod. Phys. **87**, 1213 (2015).

[4] L. Liu, C.-F. Pai, Y. Li, H. W. Tseng, D. C. Ralph, and R. A. Buhrman, Science **336**, 555 (2012).

[5] A. B. Yu and E. I. Rashba, J. Phys. C: Solid State Phys. **17**, 6039 (1984).

[6] A. Manchon and S. Zhang, Phys. Rev. B **79**, 094422 (2009).

[7] I. M. Miron, K. Garello, G. Gaudin, P. J. Zermatten, M. V. Costache, S. Auffret, S. Bandiera, B. Rodmacq, A.

Schuhl, and P. Gambardella, Nature (London) **476**, 189 (2011).
[8] W. Zhang, W. Han, X. Jiang, S.-H. Yang, and S. S. P. Parkin, Nat. Phys. **11**, 496 (2015).
[9] J. C. Rojas-Sánchez, N. Reyren, P. Laczkowski, W. Savero, J. P. Attané, C. Deranlot, M. Jamet, J. M. George, L. Vila, and H. Jaffrès, Phys. Rev. Lett. **112**, 106602 (2014).
[10] A. Chernyshov, M. Overby, X. Liu, J. K. Furdyna, Y. Lyanda-Geller, and L. P. Rokhinson, Nat. Phys. **5**, 656 (2009).
[11] R. Yoshimi, K. Yasuda, A. Tsukazaki, K. S. Takahashi, M. Kawasaki, and Y. Tokura, Sci. Adv. **4**, eaat9989 (2018).
[12] P. Wadley, B. Howells, J. Železný, C. Andrews, V. Hills, R. P. Campion, V. Novák, K. Olejník, F. Maccherozzi, S. S. Dhesi *et al.*, Science **351**, 587 (2016).
[13] S. Y. Bodnar, L. Šmejkal, I. Turek, T. Jungwirth, O. Gomonay, J. Sinova, A. A. Sapozhnik, H. J. Elmers, M. Kläui, and M. Jourdan, Nat. Commun. **9**, 348 (2018).
[14] M. Jiang, H. Asahara, S. Sato, T. Kanaki, H. Yamasaki, S. Ohya, and M. Tanaka, Nat. Commun. **10**, 2590 (2019).
[15] S. Sun, C. B. Murray, D. Weller, L. Folks, and A. Moser, Science **287**, 1989 (2000).
[16] See Supplemental Material at http://link.aps.org/supplemental/10.1103/PhysRevB.101.220402 for sample details, structural and magnetic properties, multilevel switching, SOT switching in CoPt, Joule heating effect, thermoelectrical effect, symmetry of SOT, and composition gradient details, which includes Refs. [22,25,26].
[17] C.-F. Pai, L. Liu, Y. Li, H. W. Tseng, D. C. Ralph, and R. A. Buhrman, Appl. Phys. Lett. **101**, 122404 (2012).
[18] L. Liu, O. J. Lee, T. J. Gudmundsen, D. C. Ralph, and R. A. Buhrman, Phys. Rev. Lett. **109**, 096602 (2012).
[19] S. Chen, J. Yu, Q. Xie, X. Zhang, W. Lin, L. Liu, J. Zhou, X. Shu, R. Guo, Z. Zhang *et al.*, ACS Appl. Mater. Interfaces **11**, 30446 (2019).
[20] L. Liu, Q. Qin, W. Lin, C. Li, Q. Xie, S. He, X. Shu, C. Zhou, Z. Lim, J. Yu *et al.*, Nat. Nanotechnol. **14**, 939 (2019).
[21] K.-S. Lee, S.-W. Lee, B.-C. Min, and K.-J. Lee, Appl. Phys. Lett. **102**, 112410 (2013).
[22] K. Garello, I. M. Miron, C. O. Avci, F. Freimuth, Y. Mokrousov, S. Blügel, S. Auffret, O. Boulle, G. Gaudin, and P. Gambardella, Nat. Nanotechnol. **8**, 587 (2013).
[23] J. Kim, J. Sinha, M. Hayashi, M. Yamanouchi, S. Fukami, T. Suzuki, S. Mitani, and H. Ohno, Nature Mater. **12**, 240 (2013).
[24] M. Hayashi, J. Kim, M. Yamanouchi, and H. Ohno, Phys. Rev. B **89**, 144425 (2014).
[25] C. O. Avci, K. Garello, M. Gabureac, A. Ghosh, A. Fuhrer, S. F. Alvarado, and P. Gambardella, Phys. Rev. B **90**, 224427 (2014).
[26] C. O. Avci, A. Quindeau, C.-F. Pai, M. Mann, L. Caretta, A. S. Tang, M. C. Onbasli, C. A. Ross, and G. S. D. Beach, Nature Mater. **16**, 309 (2017).
[27] X. Zhang, Q. Liu, J.-W. Luo, A. J. Freeman, and A. Zunger, Nat. Phys. **10**, 387 (2014).
[28] K. F. Dong, H. H. Li, and J. S. Chen, J. Appl. Phys. **113**, 233904 (2013).
[29] D.-H. Kim, M. Haruta, H.-W. Ko, G. Go, H.-J. Park, T. Nishimura, D.-Y. Kim, T. Okuno, Y. Hirata, Y. Futakawa *et al.*, Nature Mater. **18**, 685 (2019).